Developmental maturation of frontal cortical circuits impacts decision-making

Kevin Mastro[1-3], Wen-Chun Lee[2], Wengang Wang[2-3], Beth Stevens[2-4], Bernardo Sabatini*[1, 3-4]

1 Department of Neurobiology, Harvard Medical School, Boston, MA 02115, USA

2 F. M. Kirby Neurobiology Center, Boston Children's Hospital, Boston, MA 02115, USA

3 Stanley Center at the Broad Institute at MIT and Harvard, Cambridge, MA 02139, USA

4 Howard Hughes Medical Institute, Boston, MA 02115, USA

* Correspondence: bernardo_sabatini@hms.harvard.edu

Abstract

In humans, frontal cortical circuit maturation parallels the development of higher cognitive functions and is estimated to occur over the course of 15-20 years. In mice, frontal association cortex (FAC) maturation occurs over the first 6-8 weeks with limited reports on changes after sexual maturation (~7-8 weeks). Here we characterize frontal cortical circuits in mice across the first 6 months of life and uncovered cell-type and input-specific circuit refinement over this period, including a large increase in synaptic inhibition onto pyramidal cells relative to excitation. In parallel, we find age-related differences in the acquisition and execution of a FAC-dependent probabilistic 2-armed bandit task (2-ABT). Specifically, 4–6 month-old acquire the task more slowly and use different behavioral strategies to obtain rewards compared to younger mice. Lastly, we show that dampening the inhibitory activity in the FAC alters this behavior in a manner that counteracts the age-related differences. Together, these data present evidence for an extended period of structural synaptic maturation in FAC that directly impacts age-related changes in decision-making.

Introduction

Frontal cortical circuit maturation is a protracted process that extends into the 2nd and 3rd decade of human life and parallels the development of higher cognitive functions[1], such as goal-directed decision-making[2]. Structural maturation includes synaptic formation (birth to 10-12 years old) followed by synaptic pruning and maturation (12 to 20-25 years)[3, 4] and increased myelination and structural[5, 6] and functional[7, 8] connectivity. Over the same period, cognitive maturation is reflected in increased executive function and abstract reasoning[9-11] and reduced impulsivity[12, 13] which impact goal-directed decision-making[2]. Moreover, perturbations of frontal cortical structure are implicated in cognitive deficits found in psychiatric[14-18] and degenerative diseases[19, 20]. Nevertheless, the extent and time course of neurotypical age-dependent changes in the structure and function of cerebral cortex in mice is an active area of exploration.

Age-dependent maturation of mouse frontal association cortex (FAC) maturation occurs across the first 6-8 weeks of life. Structural changes includes increased synaptic density[21] and changes to both GABAergic[22, 23] and dopaminergic systems[24]. Consistent with data from humans, lesions to mouse FAC[25] and developmental manipulation of its inputs[26, 27] or local circuitry [28] perturb cognition, including goal-directed decision-making. Although the degree of homology of mouse and human FAC is contentious [29, 30], the FAC in both species is demarcated, in part, by the innervation of the mediodorsal thalamus (MD). MD inputs are developmentally regulated (see review[31]), contribute to higher cognitive functions and their manipulation affects decision-making[26, 32]. Therefore, refinement of MD input may contribute to protracted development of mouse FAC.

A second candidate is the development of the local GABAergic network, whose maturation in sensory areas is thought to contribute causally to the opening and closing of critical periods[33]. In sensory critical periods, distinct sources of inhibition mature at different rates and contribute to the postnatal sculpting of neural circuits[34]. Fast-spiking interneurons (FSIs) are key regulators of the network that display behaviorally relevant patterns of activity and age-dependent cellular and molecular changes. Parvalbumin (PV) positive FSIs are critical regulators of sensory critical period such that disruption to their development impedes sensory development. Consistent with these findings, developmental manipulations of FSI activity can either disrupt cognition or is a target for potential therapeutic intervention in mouse model of human disease[35]. Together, these findings suggest that the maturation of local interneuron populations may contribute to the developmental maturation of the FAC.

Here, we aim to delineate the extent for circuit and behavioral changes after the onset of sexual maturation. Utilizing slice whole-cell electrophysiology and optogenetics, we uncovered a reorganization of inputs (thalamic and intracortical) that tilts the balance between excitatory and inhibitory inputs in the favor of a greater inhibitory engagement with increasing age. In parallel, we found differences in the acquisition and execution of the FAC-dependent task and that adult level performance could be counteracted by dampening the inhibitory tone in FAC. Together, these data challenge the time period and extent of structural and behavioral changes associated with the maturation of frontal cortical circuits.

Results

To establish the time course for changes in connectivity in mouse FAC, we analyzed whole-cell electrophysiological recordings from Layer 2/3 (l2/3) pyramidal neurons in the prelimbic region of the frontal association cortex (FAC) **(Figure 1a-b)**. Consistent with anatomical and electrophysiologic evidence for an increase in spine density of l2/3 pyramidal neurons over the first 5 weeks of life [21], the frequency of miniature excitatory postsynaptic currents (mEPSCs, in the presence of TTX) increases from postnatal days (p)15-20 to P39-45 **(Figure 1c)**. However, following this peak, it decreases at p60-100 and p120-160 **(Figure 1b-c)**. In contrast, mEPSC amplitude increases until, and is maintained after, p39-45 **(Supplementary Figure 1a-b)**. Changes in the amplitude of mEPSCs typically reflect post-synaptic modifications, such as greater AMPA-type glutamate receptor (AMPAR) insertion, whereas changes in frequency suggest alterations in the number of AMPAR-containing functional synapses due to either increases in synapse number, probability of neurotransmitter release, or the fraction of synapses that contain AMPARs (i.e., that are not silent)[36].

To assay for changes in evoked synaptic transmission in FAC, a stimulating electrode was placed 500 µm from pia and the stimulation intensity was adjusted to establish a threshold stimulus that generated a 25-150 pA excitatory response in the post-synaptic l2/3 pyramidal neuron **(Figure 1d)**. We found no difference in the relationship between threshold intensity and the range of minimally evoked responses (Figure 1e-f) across age. As stimulation intensity increased, the amplitude of evoked EPSC was significantly higher for p60-100 as compared to p120-160 **(Figure 1h)**. In contrast, the maximally evoked current for p39-45 was greater than p15-30, consistent with the changes seen in mEPSCs **(Supplementary Figure 1c-d)**. The magnitude of evoked inhibitory currents was greater for p60-100 compared to p120-160 **(Figure**

1g, 1i). Series resistance and membrane capacitance were similar across groups, but cellular input resistance is significantly higher at p120-160 **(Supplementary Figure 1e-g)**, suggesting additional changes in cell size and passive properties**.**

To compare synaptic properties across the four age groups, we normalized the amplitude of evoked responses to that of the average threshold response per group which, despite our best efforts, varied across the groups. p39-45 recruits the greatest amount of excitatory drive followed by P60-100 as compared to all other groups **(Supplementary Figure 1h)**. In contrast, using the same normalization the IPSCs do not differ across age **(Supplementary Figure 1i)**. Together, these data reveal a large-scale reorganization of the frontal cortical circuits but what features of the circuit underlie these changes remain unclear.

Mediodorsal thalamus (MD) and contralateral projecting-FAC (referred to as c-FAC) send dense inputs that synapse onto l2/3 neurons within FAC[37]. Disturbances to MD activity through lesions[32] or prolonged inhibition perturb both physiology and behavior[26]. MD innervates the PFC early in development and the number of FAC-projecting thalamic neurons reduce dramatically over early development in both humans[38] and rodents[39]. Therefore, we hypothesized that changes to MD inputs may contribute to the decreases in the frequency of mEPSCs and amplitude of electrically-evoked responses. To study MD inputs in isolation, we stereotaxically delivered an AAV driving the expression of channelrhodopsin (ChR2) into MD and, 7-10 days later, prepared acute slices of FAC to examine optogenetically evoked EPSCs and disynaptic (i.e., feedforward) IPSCs in l2/3 pyramidal neurons **(Figure 2a & Supplementary Figure 2d)**.

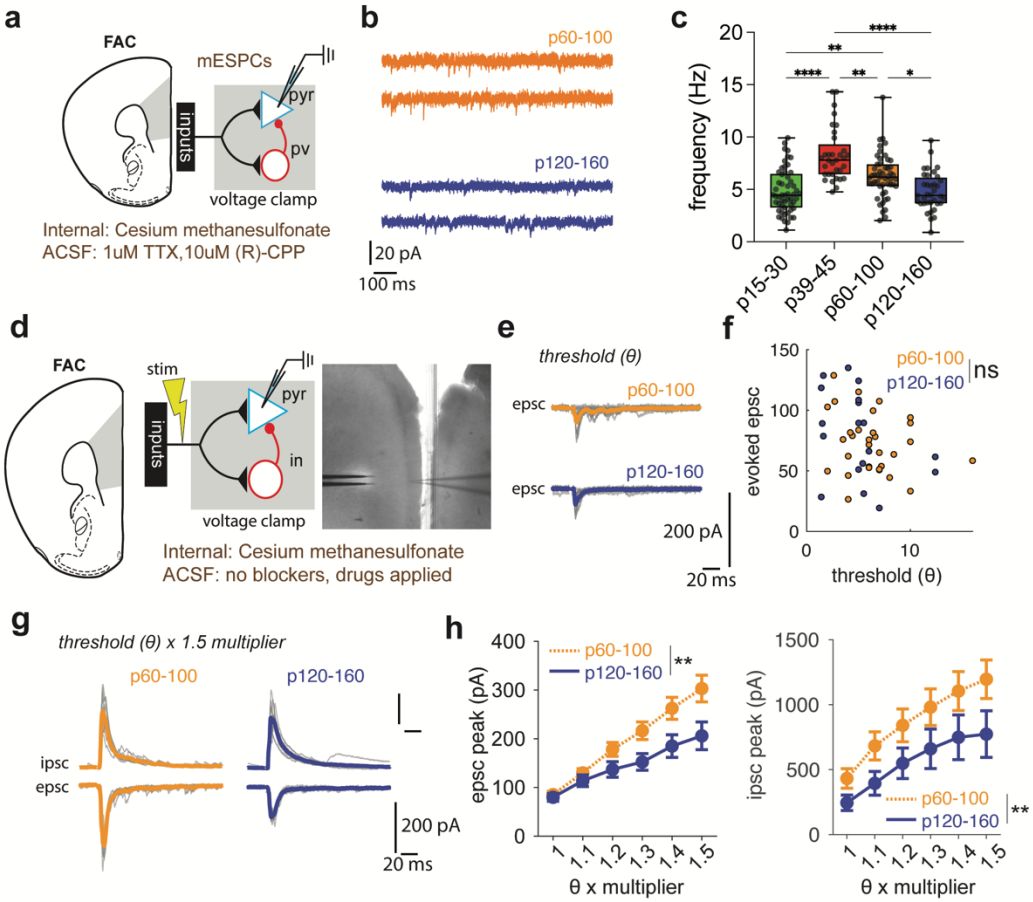

Figure 1 Protracted refinement of excitatory drive onto l2/3 pyramidal neurons in the frontal association cortex (FAC)

a) Schematic of configuration for recording mEPSCs from L2/3 pyramidal (pyr) neurons.

b) Representative traces of miniature excitatory postsynaptic current (mEPSC) recordings from cells at two of the four ages analyzed.

c) Frequency of mEPSCs shown as boxplots (median, whiskers show the full range of data) with each datapoint superimposed ($n_{p15\text{-}30} = 54$, $n_{p39\text{-}45} = 33$, $n_{p60\text{-}100} = 51$ & $n_{p120\text{-}160} = 36$ cells), one-way ANOVA was performed (Kruskal Wallis test statistic = 40.48; $p < 0.0001$) with tests for multiple comparisons (* $p < 0.02$, ** $p = 0.0089$, **** $p < 0.0001$)

d) Schematic of stimulation and recording configuration in L2/3 pyr neurons with (inset, right) low-magnification image of stimulator (two-prong) and recording electrode in FAC. bipolar concentric electrode was placed 500um from pia and (inset, bottom)

e) Representative traces (average overlaid) of evoked EPSC response at threshold (theta)

f) Evoked synaptic current peak for threshold vs. the stimulation intensities for each individual cell across the two ages ($n_{p60\text{-}100} = 31$ & $n_{p120\text{-}160} = 18$ cells). ANCOVA was performed and found no difference in threshold ($p = 0.283$), age ($p = 0.389$) or the interaction of the two ($p = 0.435$).

g) Representative traces (average overlaid) of excitatory (epsc) vs inhibitory (ipsc) postsynaptic currents, each cell was held at – 70 mV or 0 mV, respectively.

h) Evoked synaptic current peak from threshold to threshold x 1.5 multiplier shown for EPSCs (left) and IPSCs (right) ($n_{p60\text{-}100} = 31$ & $n_{p120\text{-}160} = 18$ cells). Average +/- standard error of the mean shown. Two-way ANOVA with repeated measures was performed ($p < 0.001$)

We focused on analysis of mice before (p40-60) the observed reduction in mEPSC frequency or after the reduction had stabilized (p120-160). With the highest laser power, MD-evoked EPSCs is significantly higher at p40-60 than at p120-160, while IPSCs are unchanged **(Figure 2b-c)**. These data suggest an overall decrease in the MD projection strength into the l2/3 pyramidal neurons.

c-FAC sends dense projections to Layer 3 intratelenchepalic (IT) neurons, but the changes in these projections across development have not been explored. Following injections of AAV driving expression of ChR2 into c-FAC, we recorded in l2/3 pyramidal neurons in the contralateral hemisphere **(Figure 2d & Supplementary Figure 2g)**. Optogenetic stimulation of inputs from c-FAC revealed a decrease in amplitude for excitation across varying laser powers whereas inhibition was reduced at only one intensity from P40-60 to P120-160 **(Figure 2e-f)**.

In both cases, we observed a reduction in the excitatory drive without a corresponding change in inhibition **(Supplementary Figure 2a).** To quantify the ratio of excitation and inhibition across age, we divided the amplitude of the EPSC by the sum of the amplitudes of the EPSC and IPSC (referred to as *R*). The IPSCs and EPSCs evoked by electrical stimulation have similar amplitude at p15-30 (R~0.5). However, the excitation fraction decreases at P39-49 before increasing again in the two subsequent time periods **(Supplementary Figure 2b).** For both optogenetically triggered synaptic currents from MD and c-FAC, the amplitude of evoked excitation decreases with age while inhibition stays largely unchanged, but the change in R was input-dependent. MD-evoked activity led to the identical *R* across ages while c-FAC-evoked activity led to an increase in *R* with age **(Supplementary Figure 2e, h).** These results provide evidence for pathway specific changes in the ratio of excitatory to inhibitory synaptic currents.

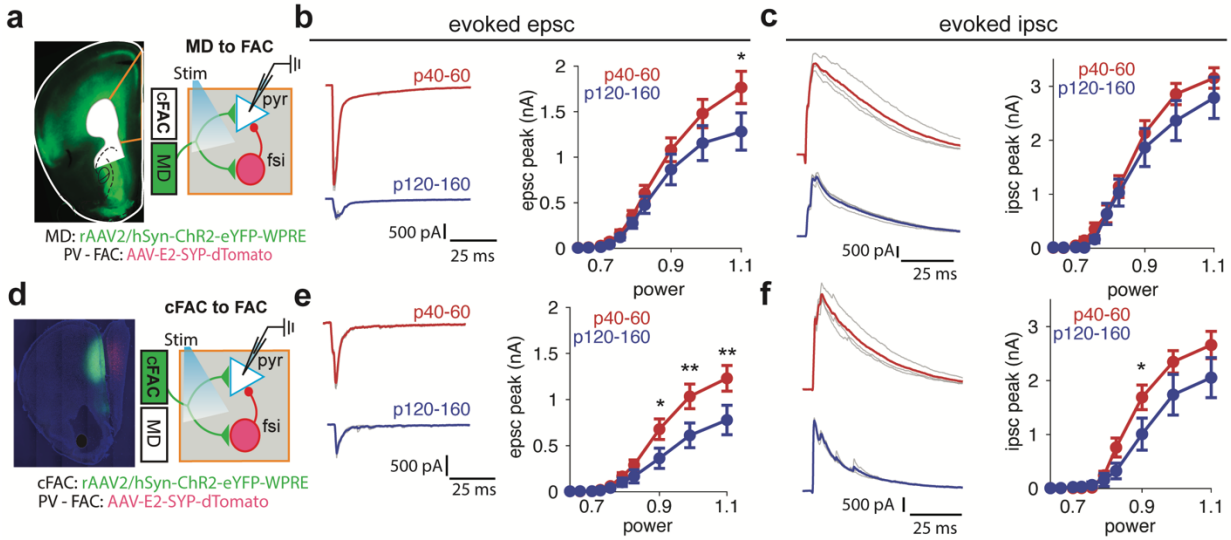

Figure 2 Pathway specific refinement of excitatory drive onto l2/3 pyradmial neurons

a) Schematic of optogenetic stimulation and recording configuration with (inset, left) low-magnification image of mediodorsal thalamic (MD) axonal expression in the FAC and (inset, right) recording L2/3 pyr neurons.

b) Representative traces (average overlaid) of excitatory (epsc) postsynaptic currents (each cell was held at –70 mV) and the evoked synaptic current peak from low to high laser power across ages ($n_{p40\text{-}60}$ = 31 & $n_{p120\text{-}160}$ = 19 cells). Average +/- standard error of the mean shown. Two-way repeated measures ANOVA was performed ($p = 0.186$) with tests for multiple comparisons (* $p < 0.02$)

c) Representative traces (average overlaid) of inhibitory (ipsc) postsynaptic currents (each cell was held at 0 mV) and the evoked synaptic current peak from low to high laser power across ages ($n_{p40\text{-}60}$ = 31 & $n_{p120\text{-}160}$ = 19 cells)**.**. Average +/- standard error of the mean shown. Two-way repeated measures ANOVA was performed ($p = 0.3487$).

d) Schematic of optogenetic stimulation and recording configuration with (inset, left) low-magnification image of contralateral frontal association cortex (c-FAC) axonal expression in the FAC and (inset, right) recording L2/3 pyr neurons.

e) Representative traces (average overlaid) epscs (each cell was held at – 70 mV) and the evoked synaptic current peak from low to high laser power across ages ($n_{p40\text{-}60}$ = 19 & $n_{p120\text{-}160}$ = 17 cells). Average +/- standard error of the mean shown. Two-way repeated measures ANOVA was performed ($p = 0.053$) with tests for multiple comparisons (* $p = 0.038$, ** $p < 0.002$)

f) Representative traces (average overlaid) of ipscs (each cell was held at 0 mV) and the evoked synaptic current peak from low to high laser power across ages ($n_{p40\text{-}60}$ = 19 & $n_{p120\text{-}160}$ = 17 cells)**.** Average +/- standard error of the mean shown. Two-way repeated measures ANOVA was performed ($p = 0.122$) with tests for multiple comparisons (* $p = 0.0487$)

Fast-spiking interneurons (FSIs), which often express parvalbumin (PV) and CCK, have specific spiking characteristics and mediate the fast feedforward inhibition (FFI) that can be driven by MD inputs [40, 41]. We used either a transgenic (PV-cre) or viral (E2 enhancer for putative PV+) strategy to express genetically encoded fluorophores in FSIs for targeted whole-cell recordings. Current-clamp recordings confirmed that cells targeted with either approach exhibited fast-spiking characteristics. Utilizing the electrical stimulation protocol, we uncovered significant decrease in the excitatory but not the inhibitory drive onto superficial, putative FSIs (**Figure 3a-b**).

To delineate pathway specific changes of excitatory drive onto FSIs, we again utilized optogenetic-assisted mapping of both MD and c-FAC inputs. MD-evoked excitatory and inhibitory drive was significantly reduced at P120-160 as compared to at younger ages **(Figure 3c-d).** In contrast, the c-FAC evoked excitatory and inhibitory drive were unchanged **(Figure 3e-f)**. In comparing these results with the concurrently collected data in l2/3 pyramidal neurons, we found that MD and c-FAC reverse the relative magnitudes of currents evoked in each cell type. MD inputs switch from more strongly innervating pyramidal cells to FSIs whereas c-FAC increases the targeting of FSIs. Moreover, the fraction of excitatory drive over total synaptic inputs (*R*) onto FSIs was bidirectionally altered. MD-evoked activity led to decreased *R* while c-FAC increased in p120-160 as compared to p40-60 (**Supplementary Figure 2 f, i**). Through optogenetic-assisted mapping of distinct inputs, we uncovered pathway- and cell-type modifications that engage the inhibition neurons to a greater extent across aging.

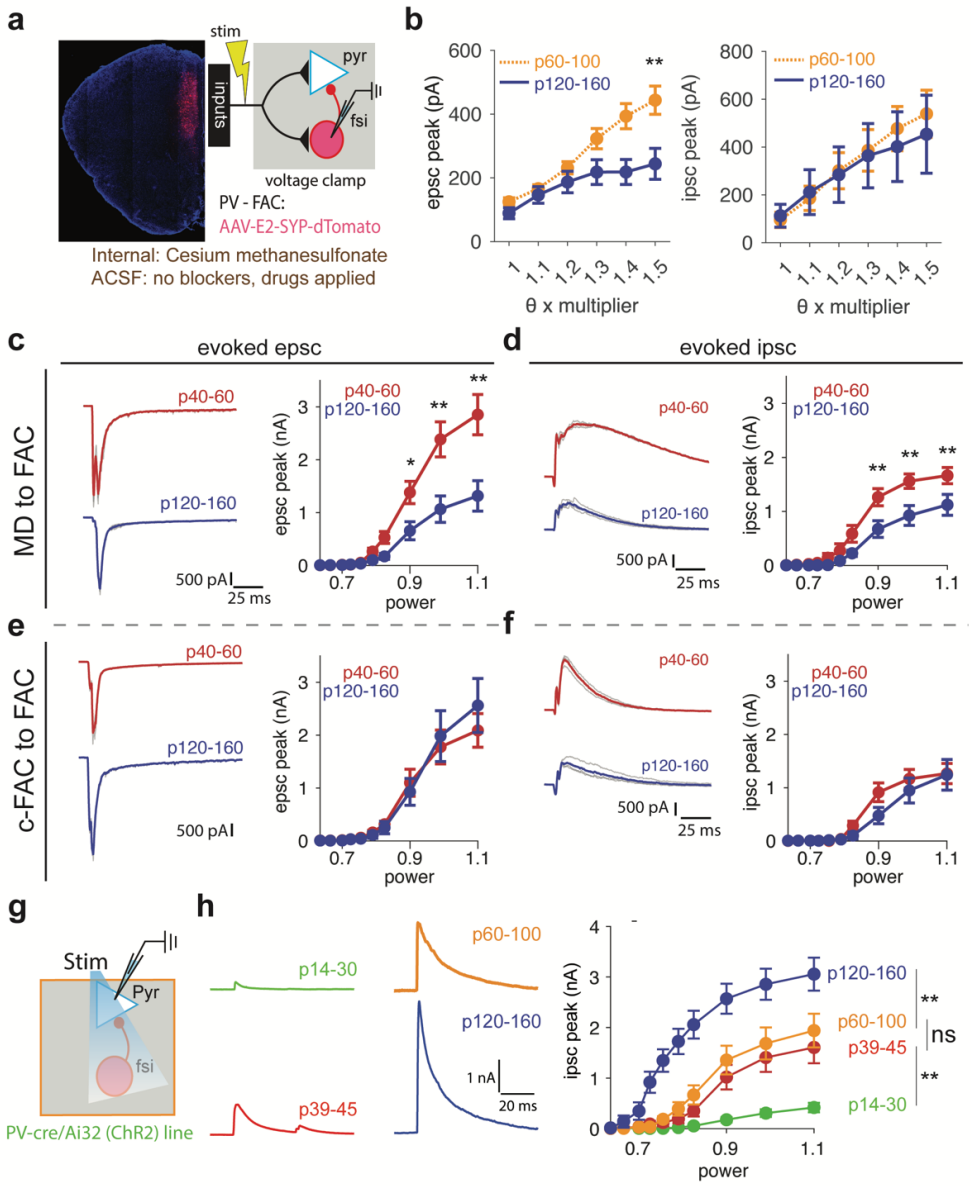

Figure 3 Protracted refinement of excitatory drive onto FSIs is pathway specific

a) Schematic of stimulation and recording configuration in fast-spiking interneurons (FSIs) with (inset, right) low-magnification image of AAV expression driving fluorophore in putative FSIs in the FAC. Stimulation provided by a bipolar concentric electrode placed 500um from pia

b) Evoked synaptic current peak from threshold to threshold x 1.5 multiplier shown for excitatory (epsc) (left) and IPSCs (right) postsynaptic currents across ages ($n_{p60\text{-}100}$ = 36 & $n_{p120\text{-}160}$ = 16 cells). Average +/- standard error of the mean shown. Two-way repeated measures ANOVA was performed (p = 0.052) with tests for multiple comparisons (* p = 0.007).

c) Representative traces (average overlaid) of epscs (each cell was held at – 70 mV) and the evoked synaptic current peak from low to high laser power across ages ($n_{p40\text{-}60}$ = 15 & $n_{p120\text{-}160}$ = 20 cells). Average +/- standard error of the mean shown. Two-way repeated measures ANOVA was performed (p = 0.002) with tests for multiple comparisons (* p = 0.010, ** p < 0.0001).

d) Representative traces (average overlaid) of ipscs (each cell was held at 0 mV) and the evoked synaptic current peak from low to high laser power across ages ($n_{p40\text{-}60}$ = 15 & $n_{p120\text{-}160}$ = 20 cells). Average +/- standard

error of the mean shown. Two-way repeated measures ANOVA was performed ($p = 0.002$) with tests for multiple comparisons (** $p < 0.0008$).

e) Representative traces (average overlaid) epscs (each cell was held at – 70 mV) and the evoked synaptic current peak from low to high laser power across ages ($n_{p40-60} = 19$ & $n_{p120-160} = 17$ cells). Average +/- standard error of the mean shown. Two-way repeated measures ANOVA was performed ($p = 0.814$).

f) Representative traces (average overlaid) of ipscs (each cell was held at 0 mV) and the evoked synaptic current peak from low to high laser power across ages ($n_{p40-60} = 19$ & $n_{p120-160} = 17$ cells). Average +/- standard error of the mean shown. Two-way repeated measures ANOVA was performed ($p = 0.318$).

g) Schematic of optogenetic stimulation and recording configuration in tissue expressing channelrhodhopsin (ChR2) driven by *cre*-expression in parvalbumin positive (PV) transgenic mice to target putative FSI axonal expression in the FAC and (inset, right) recording L2/3 pyr neurons. Average +/- standard error of the mean shown.

h) Representative traces (average overlaid) of evoked ipscs (each cell was held at 0 mV) onto l2/3 pyramidal (pyr) neurons (left) and the evoked synaptic current peak from low to high laser power (right) ($n_{p14-30} = 41$, $n_{p39-45} = 21$, $n_{p60-80} = 18$ & $n_{p120-160} = 9$ cells)**.** Average +/- standard error of the mean shown. Two-way repeated measures ANOVA was performed ($p < 0.0001$) with tests for multiple comparisons (NS $p = 0.372$, ** $p < 0.0001$)

To investigate FSI-mediated FFI, we crossed the PV-*cre* mouse line with the Ai32 line to drive expression of ChR2 in all PV cells and measured the evoked inhibitory current onto l2/3 pyramidal neurons **(Figure 3g)**. The evoked IPSC amplitude of increased from p15-20 to a similar level in both p39-45 and p60-80 **(Figure 3h)**. Then, there is a subsequent increase in the inhibitory strength from p60-80 to p120-160**(Figure 3h)**. Utilizing a transgenic approach for ChR2 expression, we found that local inhibitory drive from PV+ interneurons (putative FSIs) undergo a delayed period of maturation.

Our results indicate protracted maturation of FAC consisting of changes in long-range excitation and local inhibition which, with increasing age, results in greater relative inhibition onto l2/3 pyramidal neurons. To test whether these changes correlated with changes in a FAC-dependent behavior, mice were trained in a 2-armed bandit task (2-ABT). Mice learned to nose poke (i.e. place their snout in a port) for potential water rewards (Figure 4a). Mice must learn that at any given moment, one port is highly rewarded while the other is not. This rule will be held constant for a certain length of trials, known as a block. Therefore, at block position 0, the rule will switch, and the animal will continue to sample the previously rewarded port before switching their side choice.

To acquire the 2-ABT, mice progress through a series of 6 stages where the side ports are either rewarded or unrewarded. These stages adjust the time to make a center to side selection ('Decision Window) from 15 seconds to 2 seconds and reduce the number of trials that a rule is held constant ('block length') **(Supplementary Table 1)**. To complete acquisition, mice must execute a center to side poke selection within 2 seconds and accumulate 200 rewards within a given session. In doing so, we find that younger mice, p60-100, are capable of acquiring the task at a faster rate than the older mice, p120-180 month old **(Figure 4b)**.

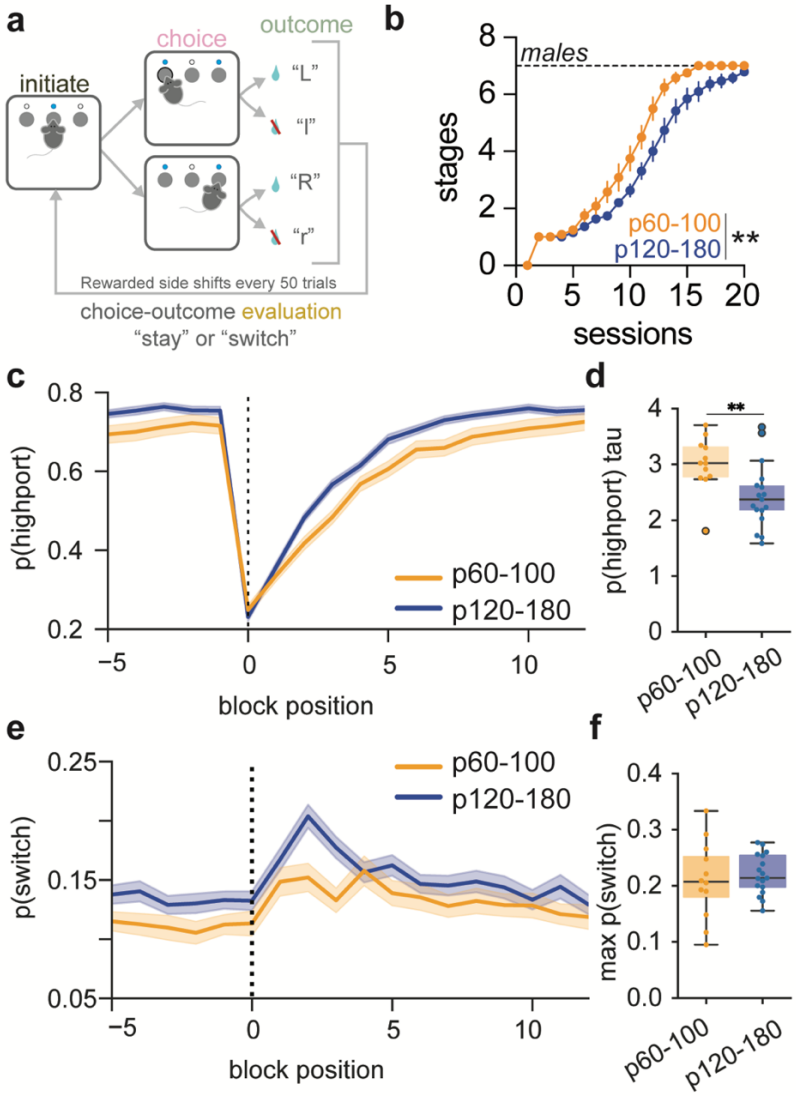

Figure 4 Age related differences in both acquisition and execution of a 2-armed bandit task
a) Schematic representation of task structure. Mice must initiate trial with nose poke in the center port followed by a side choice selection that is followed by an outcome. Highly rewarded port is held constant for a variable length of trials ('block') before the rule is reversed.
b) Proportion of mice progressing from stage 1 to 7 across daily sessions of training (~30 mins/session) across two ages ($n_{p60\text{-}100}$ = 12 & $n_{p120\text{-}180}$ = 18 mice). Two-way repeated measures ANOVA was performed (p = 0.001).
c) Probability of selecting the highly rewarded port (p(high-port)) at each trial position before (-5 to -1), after (1-12) and at a rule change (block position = 0)
d) Boxplots (median, whiskers show full range) displaying the tau (decay rate) related to the change in behavior from previously rewarded to the presently highly rewarded port (**p = 0.011, Student's t-test)
e) Probability of switching the side choice (p(switch) at each trial position before (-5 to -1), after (1-12) and at a rule change (block position = 0)
f) Boxplots (median, whiskers show full range) displaying the maximum probability of switching within a block

After acquisition, mice progressed to the evaluation phase in which the probability of a rewarding action is 80% on the highly rewarded port ($p_{(high\text{-}port)} = 0.8$) and 20% on the lowly rewarded port ($p_{(low\text{-}port)} = 1 - p_{(high\text{-}port)} = 0.2$). During the final five sessions of execution, the probability of selecting the highly rewarded port is significantly higher in p120-180 as compared to P60-100, relative to the block transitions **(Figure 4c)**. We fit the probability of choosing the highly rewarded port after the block transition with exponential and calculate the rate of decay (i.e., tau). We find that p60-100 have a larger tau, consistent with slower update of behavior **(Figure 4d)**. We also examined the probability of switching across the block and found that p60-100 switch ports less often and p120-160 show a larger increase in switching around block transitions **(Figure 4e).** Therefore, whereas all mice are capable of a higher switch probability (max p(switch)), the P120-180 concentrate these high switching periods around the block change **(Figure 4f)**. Overall, this leads to a greater reward rate for the p120-180 mice as compared to P60-100 and was reflected in the rate at which selected the highly reward port (**Figure 5a**).

Since our functional analyses revealed a protracted period of synaptic refinement during which inhibition in FAC increases and behavior in the 2ABT changes, we hypothesized that the increased inhibition drives the behavioral differences. To test this hypothesis, we injected an AAV driving the expression of an inhibitory DREADDs receptor (hM4Di) under the enhancer element (E2) to selectively target putative FSIs (**Figure 5b**). We trained these injected adult mice (p120-180) until they completed 15 sessions at the expert level and achieved a similar level of performance in the task (**Figure 5c**). Next, we administered the potent DREADDs receptor antagonist, deschloroclozapine (DCZ: 1-3 mg/ml) 30 minutes prior to each subsequent session. We find that blunting the inhibition in FAC counteracts the rate of selecting the highly rewarding port (**Figure 5d**).

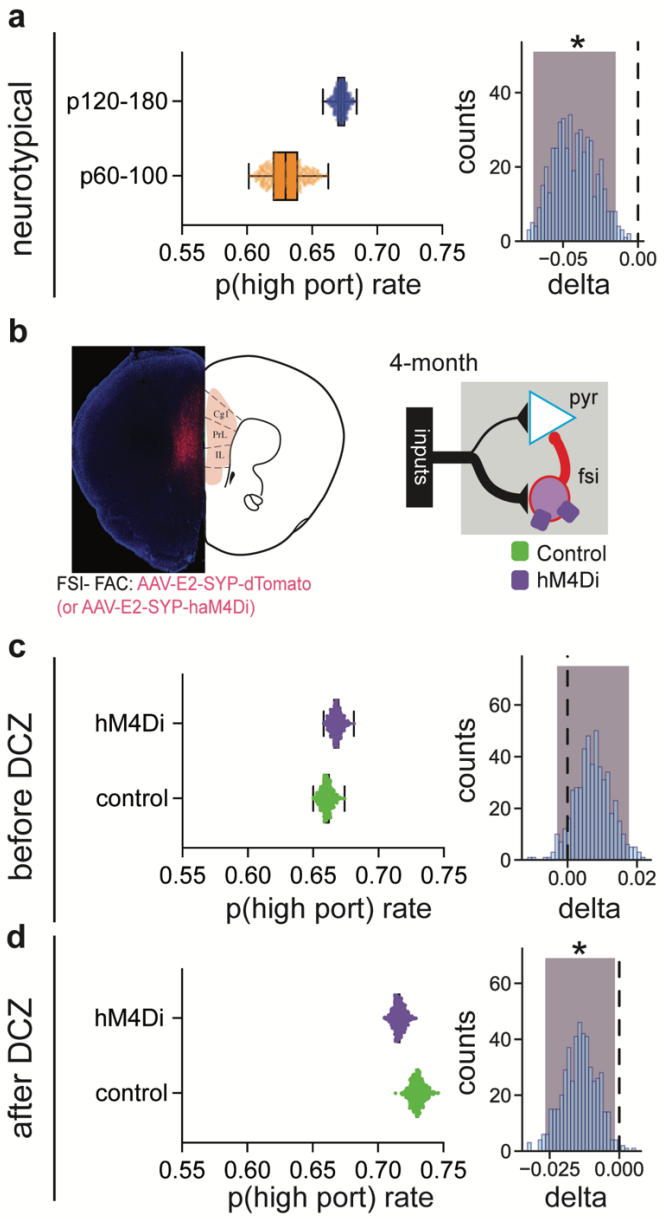

Figure 5 Decreased inhibition reverses age-related changes in 2-armed bandit task
a) Bootstrapped probabilities of selecting the highly rewarding port (p(highport) rate) (left) and the difference between (delta, right) across ages (delta = p60-100 - p120-180; $p < 0.002$)
b) Representative image (inset, left) of frontal association cortical (FAC) expression of AAV driving either fluorophore (dTomato) or inhibitory DREADDs receptor (HM4Di) under the synapsin (SYP) promotor and with the putative fast spiking interneuron (FSI) enhancer (E2). Schematic of receptor expression (inset, right) in the FSIs and not in pyramidal neurons.
c) Bootstrapped p(high port) rate (left) and the difference between (delta, right) in HM4Di and control mice before administration of deschloroclozapine (DCZ) ($p = 0.074$)
d) Bootstrapped p(high port) rate (left) and the difference between (delta, right) in HM4Di and control mice after administration of DCZ (1-3 mg/ml) via intraperitoneal injection 30-minutes prior to each session ($p = 0.012$)

Conclusions

We find that the mouse frontal cortical circuits undergo a protracted period of maturation defined by changes in excitatory and inhibitory inputs onto l2/3 pyramidal neurons and FSIs. These changes are a results of pathway specific refinement (thalamic and intracortical) that alter their cell-type preference over the course of the first 6 months of life. Together, with an increase in the local inhibitory strength, we found that the refinement led to a greater engagement of the inhibitory subnetwork. Behaviorally, we found age-related differences in both acquisition and execution of a probabilistic 2-ABT. We found that 2-month old mice were faster to acquire the 2-ABT than their older counterparts. Moreover, during execution, 2-month old mice settled on a distinct behavioral strategy where they switched their behavior after a lose more often than 6-mo old animals which overall, led to less time spent sampling the highly rewarded port. Subsequent chemogenetic inhibition of FSIs in 6-month old mice regressed their behavior back to a similar strategy to the 2-month old mice. Thus, FAC inhibition contributes to age-related changes in behavior that extends the timeline for circuit refinement and development of the FAC.

Shifting the excitatory and inhibitory landscape

The protracted development of human frontal cortex includes a decrease in excitatory inputs and an increasing amount of GABA-mediated inhibition. Together, these data suggest a greater level of inhibitory tone that has been postulated to contribute to a refinement of higher cognitive functions. The extent to which individual inputs contribute to the balance of between the two forces is still up to debate. Does an individual neuron modulate their balance to achieve a certain level of activity or are they integrative units that are balance their inputs across a much larger

network? Visual cortex equalized the balance of excitation and inhibition across pyramidal neurons[42], so then, perhaps, the same distribution applies in frontal cortex.

These data provide a systematic approach to dissecting the contribution of distinct inputs to the network balance. In addition to the MD and c-FAC, FAC receives inputs from other cortical areas, ventromedial thalamus, amygdala, hippocampus and VTA neurons, each playing a critical functional role and contribute to complex circuit motifs. Moreover, the FAC contains additional laminar organization with a rich set of interneurons who may change over this period. Future experiments must uncover how other cell-types are shifting their inputs and if there are similar stages of development that have been observed in sensory regions. For example, somatostatin interneurons mature at a different rate than their parvalbumin positive counterparts and so we would hypothesize that a similar process is taking place in FAC. Second, dopaminergic innervation and the expression of specific receptor subtypes change during human FC maturation implicated in maturing reward processing systems.

Decision-making as a tool for brain network analysis

All living beings must make decisions. Decision-making is a complex interplay between action selection and a value estimation of outcome in which an agent must incorporate their past experiences with the balance to acquire new information. Frontal cortex and associated circuits integrate homeostatic signals with motivational state and information about both current and past experiences where damage to specific regions alter these components that underlie the decision-making process. From an evolutionary perspective, the frontal cortex has undergone the greatest expansion within mammals and while primates have the most sophisticated frontal cortex, the

development of the frontal cortex has been observed in many other species. Although the rodent frontal cortex lacks the regionalization found in humans and even some anatomical attributes (lacks granularity), the rodent frontal cortex has been found to coordinate the decision-making processes. First, the rodent frontal cortex has a similar pattern of connectivity with thalamus and other subcortical regions found in the primate frontal cortex. Second, lesions to distinct regions lead to abnormalities in the decision-making process. Lastly, consistent with observations in humans, changes to frontal cortical structure and function are implicated in changing the decision-making process during both development, diseases and degeneration.

Linking Synapses to Behavior: Implications on Normative Aging

To understand how both structural and functional programs drive development, a crucial next step is to investigate the genetic programs underlying developmental maturation. Emerging genetics of Schizophrenia and other mental illnesses implicate synaptic and neuroimmune proteins[43-45]. A growing body of literature highlights non-neuronal contributions to frontal cortical maturation. Microglial and astrocytic pruning of synapses are key candidates for sculpting these circuits, while oligodendrocytes are fundamental due to their role in brain myelination. This is consistent with the increased connectivity observed in the later stages of frontal cortical maturation, where the frontal cortex (FC) is one of the last brain regions to myelinate. A systematic analysis of the transcriptomic cellular landscape across this extended period of maturation could illuminate our understanding of both neuronal and non-neuronal gene networks contributing to these structural changes.

From a top-down perspective, computational modeling provides a quantitative approach to describing underlying behaviors. By parameterizing distinct functional processes that collectively drive decision-making, we can form testable hypotheses to explain how these changes to neural circuitry impacts behavior. For instance, we hypothesize that parameters related to the storage or retrieval of previous experiences may be modulated by hippocampal inputs. By forming a holistic review of complex cognitive behaviors, we provide a foundation for inquiries into different brain abnormalities. Testing how structural alterations drive behavioral changes will inform us on how changes in these models may eventually predict the structural differences observed within individuals, thus truly linking structure to function.

Methods

All procedures were performed in accordance with the guidelines established by the National Institutes of Health and with approval from the Harvard Medical School Institutional Animal Care and Use Committee.

Animals

Male mice ranging from 2-28 weeks old on the C57BL/6J (Strain #:000664) background from Jackson Laboratory were employed for all studies. To target a fluorophore or opsin to parvalbumin-positive interneurons, we crossed the PV-Cre (Strain #: 017320) to Ai14 (dTomato, Strain #:007914) or Ai32 (ChR2: Strain #:024109) mouse lines, respectively.

Viruses

Recombinant adeno-associated viruses (AAVs with stereotypes 2/9, 5 and PHP.eB) were used to identify, monitor or manipulate cell-types utilized viral strategies in the C57BL6/Jax (Strain #:000664) mouse cohort via neuronal or PV-specific enhancer elements[46]. Most viral plasmids can be found at Addgene: AAV5-CamKII-GCaMP6f-WPRE-SV40 (no. 100834-AAV5), AAV9-hSyn-hChR2(H134R)-EYFP (no. 26973-AAV9), and AAV-PHP.eB-S5E2-dTom-nlsdTom (no. 135630-PHPeB). Some custom plasmids were packaged commercially (WZ Biosciences): AAV-PHP.eB-S5E2-hM4D(Gi)-mCherry. The E2-enhancer element provided directed expression in putatively parvalbumin-positive interneurons in frontal association cortex[46]. Upon delivery, viruses were separated into single-use aliquots (3-5 uL) and stored in the -80°C. Injection volumes ranged from 200-250nL and titers were adjusted to approximately 10^{11} to 10^{12} genomic copies per ml.

Surgery

Stereotaxic injections were performed similarly to previously reported studies[47]. Briefly, mice were anesthetized deeply using isoflurane before being placed in a stereotaxic frame where body temperature and level of anesthesia were monitored throughout the procedure. For all surgeries, the skull was exposed and the distance from bregma to lambda was used to both level and normalized for changes in skull size over the lifespan (normalization factor = measured distance (mm) /4.2 mm). Coordinates were established from bregma and a drill was used to make small craniotomies for viral injections. We used the following coordinates used for each brain area: prelimbic region of the FAC (Area 24: A/P = +1.85, M/L = +/- 0.40, D/V = -1.85) and mediodorsal thalamus (MD: A/P = -1.3, M/L = +/- 0.55 , D/V = -3.05). Pulled electrodes

containing the virus would be slowly lower to the dorsal/ventral coordinate and allowed to sit for 5 minutes. Infusion of the virus took 4-5 minutes at a rate of 50 nl/min and was followed by an additional 5 mins to counteract any flow up the injection site. After completing the injections, skin was returned and sutured and ointment was used to prevent any infection and limit inflammation.

Behavior

The two-armed bandit task (2-ABT) was consistent in both box and behavioral design as previous work[47, 48]. Briefly, mice were water regulated to 1-2 ml/day until they maintained ~80% *ad libitum* weight. On training days, mice were placed in a 4.9" x 6" acrylic chamber that contained three custom nose ports with an infrared-beam sensor (full design plans can be found on "Open Behavior").

To facilitate the acquisition of the task, mice progressed through a series of stages. As shown in **Supplementary Table 1**, parameters of the tasks were shifted until achieving the ideal task structure where decisions are made within 2 seconds ("Decision Window") where the probability of the highly rewarded port ("p(high port)") was 0.8, probability of the low rewarded port ("p(low port)") was 0.2 with a variable blocklength of 10-30 trials. For example, Stage 1 rewards the agent for any pokes in the right and left ports. This stage is necessary to acquire the relationship between a nose poke action and the reward. Stage 2 requires the agent to poke in the center port followed by side port poke and reward. This center to side association is strengthened through a combination of decreasing the amount of time allowed between the two pokes (Stage 2-5) followed by a reduction in the length of a given block (Stage 6). To complete a stage,

animals had to successfully acquire 100 rewards in a given session for each of stages 1-5 and 200 rewards for Stage 6. Upon successful acquisition of the task, mice were progressed to stage 7 where they completed 8-12 sessions of the probabilistic task. Behavioral training was completed during the dark phase of the mouse sleep/wake cycle and were run under no ambient light.

Behavioral Analysis

All metrics were based on completed trials where mice initiated a center nose poke followed by the selection of a right or left nose poke. To observe differences in training, the number of days to achieve criterion on any given stage was plotted.

To evaluate the performance on the probabilistic task, the probability that a mouse selects the highly reward port can be calculated relative to the trial position in the block. At 'Block Position' zero, the highly rewarded port switches to the other port (From left to right, or right to left) and the mouse must adapt their behavior to track the change in the task. The action of the mouse can be represented by either the probability of correctly choosing the highly-rewarded port (p(high port)) or the probability of switching (p(switch)) which would be expected to increase after block position 0.

We employed a bootstrapping approach to estimate the means and standard deviations of several behavioral metrics across conditions or age groups. For each metric, data was resampled with replacement 500 times to generate bootstrapped distributions. To quantify the differences between conditions, we calculated the delta (Δ) values by subtracting the bootstrapped estimates of the control group from those of the treatment group for each iteration (p120-180 vs p60-100 or

Control vs hM4Di, respectively). This generated a distribution of delta values, representing the pairwise differences between the two groups.

Slice physiology preparation

Coronal sections (250-300 um thickness) were prepared from brains of 5-28 weeks-old mice. First, mice were transcranially perfused with ice-cold ACSF solution (in mM): 125 NaCl, 2.5 KCl, 25 NaHCO3, 2 CaCl2, 1 MgCl2, 1.25 NaH2PO4 and 11 glucose (300–305 mOsm kg−1). Slices from the anterior portion of the mouse brain that contained prelimbic region of the FAC were prepared on a Leica VT1200 vibratome in the same ice-cold ACSF solution followed by a 5-10 min incubation period at 34 °C containing a choline-based solution (in mM): 110 mM choline chloride, 25 mM $NaHCO_3$, 2.5 mM KCl, 7 mM $MgCl_2$, 0.5 mM $CaCl_2$, 1.25 mM NaH_2PO_4, 25 mM glucose, 11.6 mM ascorbic acid and 3.1 mM pyruvic acid. The choline-based incubation is followed by an additional 15-minute incubation in ACSF at 34 °C. After the second incubation, slices were moved to room temperature and maintained for the length of the recording. All solutions were carbogenated at all stages of tissue preparation and data collection.

Slice physiology collection and analysis

General recording principals: Recordings were made at 32-34°C in carbogenated ACSF (in mM): 125 NaCl, 26 NaHCO3, 1.25 NaH2PO4, 2.5 KCl, 12.5 glucose, 1 MgCl2, and 2 CaCl2. Data was collected on and a low-pass filter was applied (MultiClamp 700B amplifier; Molecular Devices) and then digitized on a National Instruments acquisition board. Data was acquired via a custom version of ScanImage written in MATLAB. Data was analyzed offline using custom code written in Matlab or Python. Electrodes were made from borosilicate glass (pipette

resistance, 2– 4 M). Series resistance was monitored throughout the voltage clamp recordings and prior to the start of all current clamp recordings and cells were excluded if series changed greater than 20% of the initial baseline or exceeded 25 MOhm.

Voltage clamp recordings utilized a cesium-based internal (in mM): 135 $CsMeSO_3$, 10 HEPES, 1 EGTA, 3.3 QX-314 (Cl^- salt), 4 Mg^-ATP, 0.3 Na-GTP, 8 Na_2-phosphocreatine, pH 7.3 adjusted with CsOH; 295 mOsm kg^-1). For the external ACSF solution for the electrical and optogenetic experiments, no blockers were used in the external ACSF. For miniature excitatory postsynaptic (mEPSC) experiments, external ACSF contained 1 μM TTX and 10 uM CPP. Voltage-clamp recordings were filtered at 2 kHz and digitized at 10 kHz.

For mEPSC recordings, cells were held at -70 mV and monitored for 5-10 mins. Recording epochs with stable baselines and access resistance were included for analysis. To measure the frequency and amplitude of the excitatory events, we utilized custom MATLAB scripts adapted [49]and applied previously[50].

For electrical stimulation, a bipolar concentric electrode was positioned 500 um from the top of pia and recordings targeted superficial pyramidal neurons and putative fast-spiking interneurons labeled by either viral or transgenic approaches. As described previously[51], threshold (theta) was established by tuning the electrical stimulation (1 pulse @ 10 ms) until a 20-150 pA (peak magnitude) excitatory postsynaptic current was present at the -70 mV holding voltage. The threshold was then multiplied by 1.1-1.5 and responses were recorded at both -70 mV and 0 mV for each neuron. Each stimulation intensity was collected five times with a 30 second inter-

stimulation interval. For optogenetic stimulation, laser power was calibrated to the same level of laser intensity. Stimulation (1 pulse @ 3 ms) were taken at varying laser intensities and were randomly interspersed. Each laser intensity was collected three times with a 30 second inter-stimulation interval. Like electrical stimulation, cells were held at -70 mV (to isolate excitatory drive) followed by 0 mV hold (to isolate inhibitory drive). To understand how each stimulation impacted the local network, the current response for each stimulation was integrated over a 20 ms window of time (Area under the curve). To isolate the impact of monosynaptic drive, peak magnitude was analyzed within a short latency activation (<5 ms). For statistical testing, multiple unpaired t-tests adjusted for multiple comparisons were performed and both the p-value and q-value (adjusted for False Discovery Rate) are reported.

Currently clamp recordings utilized a potassium-based internal: 130 KMeSO3, 3 KCl, 10 HEPES, 1 EGTA, 4 Mg-ATP, 0.3 Na-GTP, 8 sodium phosphocreatine (pH 7.3 adjusted with KOH; 295 mOsm). For recordings of intrinsic excitability, 10 uM gabazine 10 uM NBQX and 10 uM CPP were included in the bath to block fast inhibitory and excitatory transmission, respectively. Data was filtered at 10 kHz and digitized at 40 kHz. For current-voltage relationship, current steps were applied for 500 ms from -200 to 200 pA in 20 pA steps. For current-firing rate relationship, additional steps were applied from 200-1000 pA in 50 pA steps.

Behavioral Chemogenetics

Mice underwent surgery and were randomly assigned to receive injection of HM4Di or mCherry viral vectors. Following surgical recovery and water regulation, mice completed acquisition (Stages 1-6) and 15 sessions of the probabilistic (Stage 7) of the 2-ABT. For the next 10

sessions, animals were administered the DREADDs activator deschloroclozapine (DCZ: 1-3 mg/ml) via intraperitoneal injection 30-minutes prior to completing the task[52]. Experimenters were blind to experimental conditions during data acquisition.

Histology and Imaging

Mice were deeply anesthetized with isoflurane and perfused transcardially with 20 ml of PBS followed by 10 ml of 4% paraformaldehyde (PFA). Brain was excavated and placed overnight in 4% PFA at 4ºC. Brains were transferred to 30% sucrose for equilibration and stored at 4ºC until falling to the bottom of the container. Using dry ice, brains were frozen in an optimal cutting temperature compound (O.C.T.: Tissue-Tek) and cut on the cryostat (50 um slice). DAPI mounting medium (Vectashield, H-1200) was used to preserve fluorescence quality and was imaged immediately on a widefield microscope at 10x objective. For viral verification, no enhancement of the expression was necessary.

Statistics

Statistical analysis was completed using custom MATLAB and Python scripts and Prism (GraphPad; Version 10).

Supplementary Figures

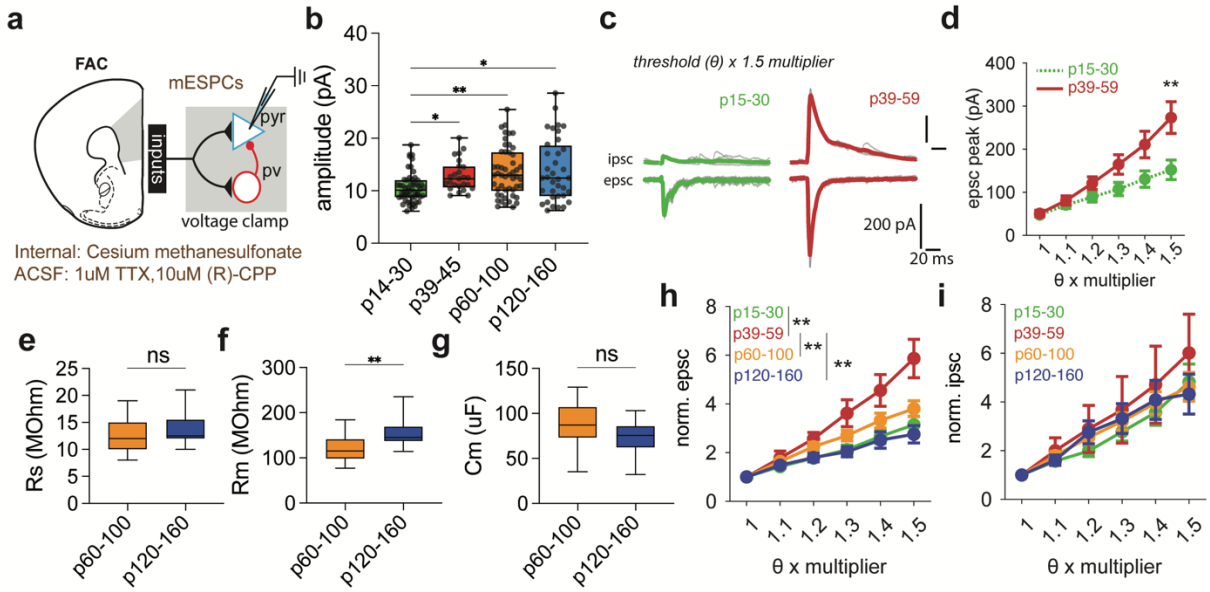

Supplementary Figure 1 Refinement of presynaptic, not postsynaptic excitatory drive onto l2/3 pyramidal neurons in the frontal association cortex (FAC)

a) Schematic of configuration for recording mEPSCs from L2/3 pyramidal (pyr) neurons.

b) Amplitude of mEPSCs shown as boxplots (median, whiskers show the full range of data) with each datapoint superimposed across ages (n_{p15-30} = 54, n_{p39-45} = 33, $n_{p60-100}$ = 51 & $n_{p120-160}$ =36 cells), one-way ANOVA was performed (Kruskal Wallis test statistic = 15.79; p = 0.0013) with tests for multiple comparisons (* p <0.02, ** p < 0.3 ** p < 0.004)

c) Representative traces (average overlaid) of evoked EPSC response at threshold (theta) x 1.5 multiplier

d) Evoked synaptic current peak for threshold vs. the stimulation intensities for each individual cell across the two ages (n_{p15-30} = 47, n_{p39-45} = 14 cells). Two-way repeated measures ANOVA was performed (p = 0.058) with tests for multiple comparisons (** p < 0.009)

e) Series resistance (MΩ) shown as boxplots (median, whiskers show the full range of data) (p = 0.354, Student's t-test)

f) Cellular input resistance (MΩ) shown as boxplots (median, whiskers show the full range of data) (p = 0.0039, Student's t-test)

g) Capacitance (µF) shown as boxplots (median, whiskers show the full range of data) (p = 0.133, Student's t-test)

h) Normalized evoked synaptic current peak from threshold to threshold x 1.5 multiplier shown for EPSCs (left) and IPSCs (right) across all four ages (n_{p15-30} = 47, n_{p39-45} = 14 cells, , $n_{p60-100}$ = 51 & $n_{p120-160}$ =36 cells) . Average +/- standard error of the mean shown. Two-way repeated measures ANOVA was performed (EPSC: p = 0.0003, IPSC: p > 0.05) with tests for multiple comparisons at threshold x 1.5 multiplier (** p < 0.0001)

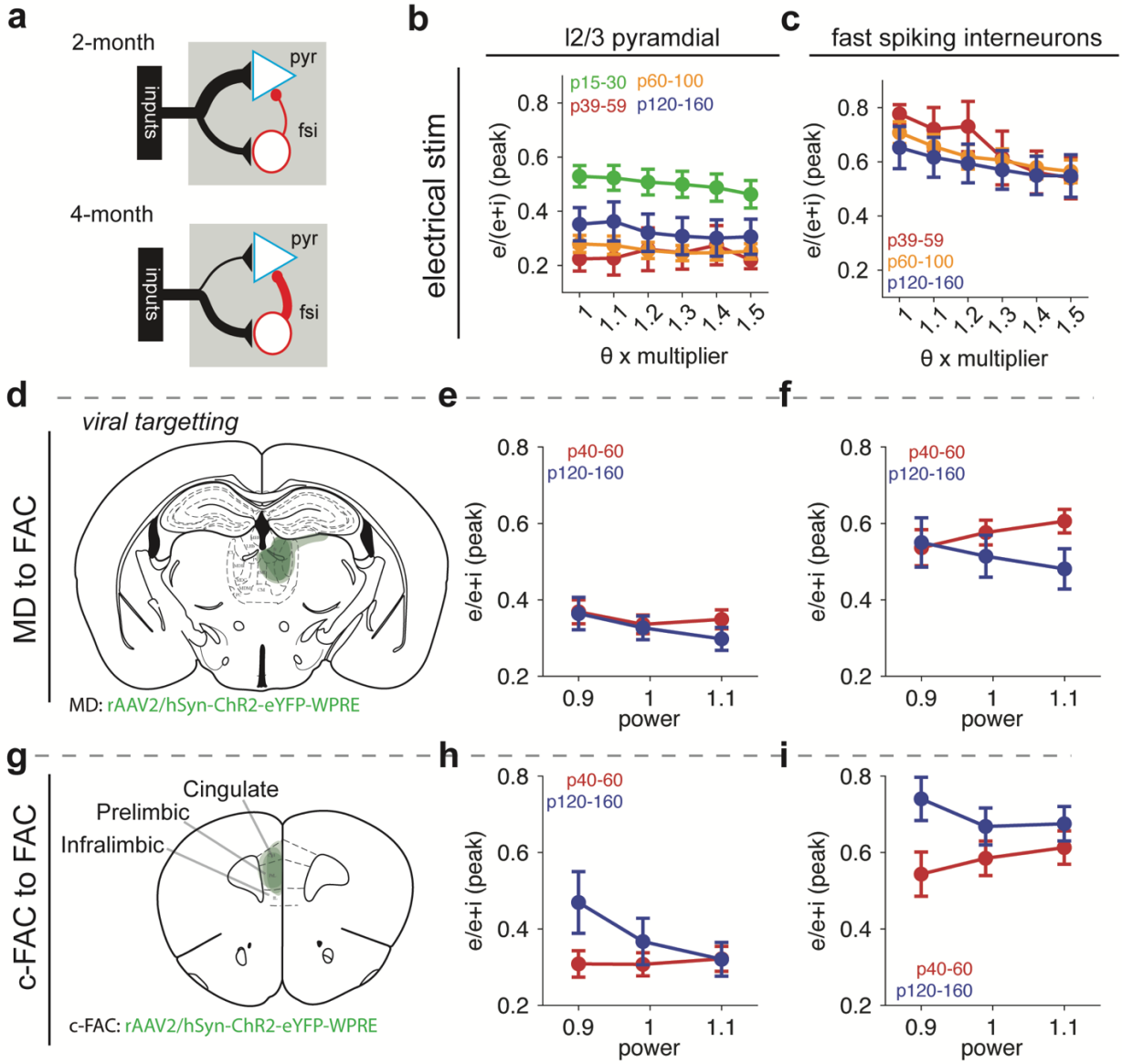

Supplementary Figure 2 Protracted refinement of excitatory/inhibitory balance drive onto l2/3 pyramidal neurons and fast spiking interneurons

a) Schematic of observed changes onto L2/3 pyramidal (pyr) neurons and fast-spiking interneurons (FSIs).
b) Fraction of excitatory (EPSC) over total synaptic inputs (EPSC+IPSC) onto L2/3 pyr (left) and FSIs (right) vs. the electrical stimulation intensities across the four ages. Average +/- standard error of the mean shown.
c) Representative viral targeting location across 3 animals in the mediodorsal thalamus (MD), injected with the AAV driving expression of channelrhodopsin (ChR2) in neurons (human synapsin (hSyn) promoter)
d) Fraction of excitatory (EPSC) over total synaptic inputs (EPSC+IPSC) onto L2/3 pyr (left) and FSIs (right) vs. the optogenetic stimulation of MD inputs across the four ages. Average +/- standard error of the mean shown.
e) Representative viral targeting location across 3 animals in the contralateral-frontal association cortex (c-FAC), injected with the AAV driving expression of ChR2 in neurons (hSyn promoter)
f) Fraction of excitatory (EPSC) over total synaptic inputs (EPSC+IPSC) onto L2/3 pyr (left) and FSIs (right) vs. the optogenetic stimulation of c-FAC inputs across the four ages. Average +/- standard error of the mean shown.

stage	decision window	p(high port)	p(low port)	blocklength
1	NA	1.0	1.0	NA
2	15	1.0	0.0	50
3	7	1.0	0.0	50
4	3	1.0	0.0	50
5	2	1.0	0.0	50
6	2	1.0	0.0	20
7	2	0.8	0.2	10-30

Supplementary Table 1: Stages of acquisition for the 2-armed bandit task (2-ABT)
Center poke followed by a side poke behavior is shaped over the course of 6 stages where experimenter shifts the amount of time to make center to side selection ('decision window' in seconds), probability of the highly rewarded (p(high port)) and lowly rewarded (p(low port)) ports and the length of trials that the rule is held constant ('blocklength'). Stage 7 represents the final stage of the 2-ABT that is used for the execution phase.

References

1. Spear, L.P., *The adolescent brain and age-related behavioral manifestations.* Neuroscience & biobehavioral reviews, 2000. **24**(4): p. 417-463.
2. Tervo-Clemmens, B., et al., *A canonical trajectory of executive function maturation from adolescence to adulthood.* Nature communications, 2023. **14**(1): p. 6922.
3. Huttenlocher, P.R., *Synaptic density in human frontal cortex - developmental changes and effects of aging.* Brain Res, 1979. **163**(2): p. 195-205.
4. Petanjek, Z., et al., *The Protracted Maturation of Associative Layer IIIC Pyramidal Neurons in the Human Prefrontal Cortex During Childhood: A Major Role in Cognitive Development and Selective Alteration in Autism.* Front Psychiatry, 2019. **10**: p. 122.
5. Miller, D.J., et al., *Prolonged myelination in human neocortical evolution.* Proc Natl Acad Sci U S A, 2012. **109**(41): p. 16480-5.
6. Giorgio, A., et al., *Longitudinal changes in grey and white matter during adolescence.* Neuroimage, 2010. **49**(1): p. 94-103.
7. Calabro, F.J., et al., *Development of hippocampal–prefrontal cortex interactions through adolescence.* Cerebral Cortex, 2020. **30**(3): p. 1548-1558.
8. Tang, L., A.T. Shafer, and N. Ofen, *Prefrontal cortex contributions to the development of memory formation.* Cerebral Cortex, 2018. **28**(9): p. 3295-3308.
9. Cromer, J.A., et al., *The nature and rate of cognitive maturation from late childhood to adulthood.* Frontiers in psychology, 2015. **6**: p. 127486.
10. Luciana, M., et al., *The development of nonverbal working memory and executive control processes in adolescents.* Child development, 2005. **76**(3): p. 697-712.
11. Luna, B., et al., *Maturation of cognitive processes from late childhood to adulthood.* Child development, 2004. **75**(5): p. 1357-1372.
12. Ordaz, S.J., et al., *Longitudinal growth curves of brain function underlying inhibitory control through adolescence.* Journal of Neuroscience, 2013. **33**(46): p. 18109-18124.
13. Quach, A., et al., *Adolescent development of inhibitory control and substance use vulnerability: A longitudinal neuroimaging study.* Developmental cognitive neuroscience, 2020. **42**: p. 100771.
14. Flynn, S.W., et al., *Abnormalities of myelination in schizophrenia detected in vivo with MRI, and post-mortem with analysis of oligodendrocyte proteins.* Mol Psychiatry, 2003. **8**(9): p. 811-20.
15. Glantz, L.A. and D.A. Lewis, *Reduction of synaptophysin immunoreactivity in the prefrontal cortex of subjects with schizophrenia. Regional and diagnostic specificity.* Arch Gen Psychiatry, 1997. **54**(10): p. 943-52.
16. Glantz, L.A. and D.A. Lewis, *Dendritic spine density in schizophrenia and depression.* Arch Gen Psychiatry, 2001. **58**(2): p. 203.
17. Goto, Y., C.R. Yang, and S. Otani, *Functional and dysfunctional synaptic plasticity in prefrontal cortex: roles in psychiatric disorders.* Biological psychiatry, 2010. **67**(3): p. 199-207.
18. Kumari, V., et al., *Cortical grey matter volume and sensorimotor gating in schizophrenia.* Cortex, 2008. **44**(9): p. 1206-14.
19. Li, M., C. Long, and L. Yang, *Hippocampal-prefrontal circuit and disrupted functional connectivity in psychiatric and neurodegenerative disorders.* BioMed research international, 2015. **2015**.
20. Narayanan, M., et al., *Common dysregulation network in the human prefrontal cortex underlies two neurodegenerative diseases.* Molecular systems biology, 2014. **10**(7): p. 743.
21. Kroon, T., et al., *Early postnatal development of pyramidal neurons across layers of the mouse medial prefrontal cortex.* Sci Rep, 2019. **9**(1): p. 5037.

22. Caballero, A., et al., *Differential regulation of parvalbumin and calretinin interneurons in the prefrontal cortex during adolescence.* Brain Structure and Function, 2014. **219**: p. 395-406.
23. Caballero, A., et al., *Emergence of GABAergic-dependent regulation of input-specific plasticity in the adult rat prefrontal cortex during adolescence.* Psychopharmacology, 2014. **231**: p. 1789-1796.
24. Tseng, K.Y. and P. O'Donnell, *Dopamine modulation of prefrontal cortical interneurons changes during adolescence.* Cereb Cortex, 2007. **17**(5): p. 1235-40.
25. Bissonette, G.B., et al., *Double dissociation of the effects of medial and orbital prefrontal cortical lesions on attentional and affective shifts in mice.* Journal of Neuroscience, 2008. **28**(44): p. 11124-11130.
26. Benoit, L.J., et al., *Adolescent thalamic inhibition leads to long-lasting impairments in prefrontal cortex function.* Nature neuroscience, 2022. **25**(6): p. 714-725.
27. Ferguson, B.R. and W.-J. Gao, *Thalamic control of cognition and social behavior via regulation of gamma-aminobutyric acidergic signaling and excitation/inhibition balance in the medial prefrontal cortex.* Biological psychiatry, 2018. **83**(8): p. 657-669.
28. Canetta, S.E., et al., *Mature parvalbumin interneuron function in prefrontal cortex requires activity during a postnatal sensitive period.* Elife, 2022. **11**: p. e80324.
29. Laubach, M., et al., *What, if anything, is rodent prefrontal cortex?* eneuro, 2018. **5**(5).
30. Le Merre, P., S. Ährlund-Richter, and M. Carlén, *The mouse prefrontal cortex: Unity in diversity.* Neuron, 2021. **109**(12): p. 1925-1944.
31. Ferguson, B.R. and W.-J. Gao, *Development of thalamocortical connections between the mediodorsal thalamus and the prefrontal cortex and its implication in cognition.* Frontiers in human neuroscience, 2015. **8**: p. 1027.
32. Ouhaz, Z., et al., *Mediodorsal thalamus is critical for updating during extradimensional shifts but not reversals in the attentional set-shifting task.* Eneuro, 2022. **9**(2).
33. Le Magueresse, C. and H. Monyer, *GABAergic interneurons shape the functional maturation of the cortex.* Neuron, 2013. **77**(3): p. 388-405.
34. Tuncdemir, S.N., et al., *Early somatostatin interneuron connectivity mediates the maturation of deep layer cortical circuits.* Neuron, 2016. **89**(3): p. 521-535.
35. Mukherjee, A., et al., *Long-lasting rescue of network and cognitive dysfunction in a genetic schizophrenia model.* Cell, 2019. **178**(6): p. 1387-1402. e14.
36. Vardalaki, D., K. Chung, and M.T. Harnett, *Filopodia are a structural substrate for silent synapses in adult neocortex.* Nature, 2022. **612**(7939): p. 323-327.
37. Little, J.P. and A.G. Carter, *Subcellular synaptic connectivity of layer 2 pyramidal neurons in the medial prefrontal cortex.* J Neurosci, 2012. **32**(37): p. 12808-19.
38. Abitz, M., et al., *Excess of neurons in the human newborn mediodorsal thalamus compared with that of the adult.* Cerebral Cortex, 2007. **17**(11): p. 2573-2578.
39. Rios, O. and J. Villalobos, *Postnatal development of the afferent projections from the dorsomedial thalamic nucleus to the frontal cortex in mice.* Developmental brain research, 2004. **150**(1): p. 47-50.
40. Delevich, K., et al., *The mediodorsal thalamus drives feedforward inhibition in the anterior cingulate cortex via parvalbumin interneurons.* Journal of Neuroscience, 2015. **35**(14): p. 5743-5753.
41. Kamalova, A., et al., *CCK+ interneurons contribute to thalamus-evoked feed-forward inhibition in prelimbic prefrontal cortex.* Journal of Neuroscience, 2024.
42. Xue, M., B.V. Atallah, and M. Scanziani, *Equalizing excitation–inhibition ratios across visual cortical neurons.* Nature, 2014. **511**(7511): p. 596-600.
43. Baum, M.L., et al., *CSMD1 regulates brain complement activity and circuit development.* Brain, Behavior, and Immunity, 2024. **119**: p. 317-332.

44. Sekar, A., et al., *Schizophrenia risk from complex variation of complement component 4.* Nature, 2016. **530**(7589): p. 177-183.
45. Singh, T., et al., *Rare coding variants in ten genes confer substantial risk for schizophrenia.* Nature, 2022. **604**(7906): p. 509-516.
46. Vormstein-Schneider, D., et al., *Viral manipulation of functionally distinct interneurons in mice, non-human primates and humans.* Nat Neurosci, 2020. **23**(12): p. 1629-1636.
47. Chantranupong, L., et al., *Dopamine and glutamate regulate striatal acetylcholine in decision-making.* Nature, 2023. **621**(7979): p. 577-585.
48. Beron, C.C., et al., *Mice exhibit stochastic and efficient action switching during probabilistic decision making.* Proc Natl Acad Sci U S A, 2022. **119**(15): p. e2113961119.
49. Merel, J., et al., *Bayesian methods for event analysis of intracellular currents.* J Neurosci Methods, 2016. **269**: p. 21-32.
50. Wilton, D.K., et al., *Microglia and complement mediate early corticostriatal synapse loss and cognitive dysfunction in Huntington's disease.* Nat Med, 2023. **29**(11): p. 2866-2884.
51. Antoine, M.W., et al., *Increased Excitation-Inhibition Ratio Stabilizes Synapse and Circuit Excitability in Four Autism Mouse Models.* Neuron, 2019. **101**(4): p. 648-661 e4.
52. Nagai, Y., et al., *Deschloroclozapine, a potent and selective chemogenetic actuator enables rapid neuronal and behavioral modulations in mice and monkeys.* Nat Neurosci, 2020. **23**(9): p. 1157-1167.